



Computational analysis of actively-cooled 3D woven microvascular composites using a stabilized interface-enriched generalized finite element method



Soheil Soghrati¹, Ahmad R. Najafi, Jie H. Lin, Kevin M. Hughes, Scott R. White, Nancy R. Sottos, Philippe H. Geubelle^{*}

Beckman Institute for Advanced Science and Technology, University of Illinois at Urbana-Champaign, 405 North Mathews Avenue, Urbana, IL 61801, USA

ARTICLE INFO

Article history:

Received 13 February 2013
Received in revised form 18 May 2013
Accepted 19 May 2013
Available online 29 June 2013

Keywords:

3D woven composite
Active cooling
Microvascular materials
Interface-enriched Generalized FEM
Convection–diffusion equation
SUPG

ABSTRACT

The computational design of an actively-cooled 3D woven microvascular composite plate with sinusoidal and straight microchannels is presented. The design objectives include minimizing the maximum temperature of the composite, the microchannel volume fraction, and the pressure drop needed to circulate the coolant in the microchannels. We study the impact of a variety of parameters on the optimal design of a microvascular composite plate subjected to a uniform heat flux over its bottom surface. These parameters include the spacing, wavelength, and amplitude of the microchannels, the coolant type and flow rate, and the applied thermal loads. To facilitate the computational design process, a mesh-independent Interface-enriched Generalized Finite Element Method (IGFEM) is employed to evaluate the temperature field in the actively-cooled composite. The IGFEM solver also includes the streamline upwind Petrov-Galerkin stabilization scheme to eliminate the spurious oscillations in the temperature field due to the convection-dominated heat transfer in the microchannels. This study reveals that the straight microchannels are often the optimal configuration. Design maps are presented to evaluate the required flow rate as a function of the applied thermal load and the plate dimensions.

© 2013 Elsevier Ltd. All rights reserved.

1. Introduction

Bio-inspired actively-cooled microvascular materials have found a variety of engineering applications, including those in biotechnology [1,2], chemical reactors [3], and micro-electro-mechanical systems (MEMS) [4–7]. Manufacturing techniques such as the direct-writing assembly allow creating microchannels with a wide range of diameters and configurations in polymeric materials [8–11]. Recently, embedding microchannels in 3D woven composites has been made possible via the vaporization of sacrificial components (VaSC) technique [12]. In this technique, some of the fiber tows in the woven preform are replaced by catalyst-impregnated polylactic acid (PLA) sacrificial fibers and infiltrated with a low viscosity resin-like epoxy. After curing the sample, the composite is heated to about 200 °C to form hollow microchannels by vaporizing and evacuating the sacrificial fibers. The configuration of these embedded microchannels depends on the weave architecture and placement of the sacrificial fibers, i.e., in the warp, weft, or through-thickness directions. Fig. 1 illustrates a 3D woven

glass fiber/ epoxy matrix microvascular composite specimen made by the VaSC technique. In this case, some through-thickness (z) fibers are replaced by PLA fibers during weaving and then removed by VaSC to form sinusoidal-shaped microchannels. Similarly, incorporating the sacrificial fibers in the warp or weft directions leads to straight microchannels.

Motivated by these recent advances in the manufacturing of microvascular composites, we present hereafter a design study of actively-cooled polymeric matrix composite (AC-PMC) plates. The epoxy matrix with glass fibers are used to create the 3D woven composite preform. We examine the impact of both sinusoidal-shape and straight embedded microchannels on the thermal response of the microvascular composite. The PMC plate is subjected to a heat flux that, in the absence of the active cooling, causes a high temperature gradient in the thickness direction and a high surface temperature, well beyond the maximum sustainable temperature of this material. Relevant novel applications include the design of lightweight skin materials for hypersonic aircrafts, where active cooling is needed to cope with high thermal loads caused by aerodynamic heating. The objective of this work is to determine the optimal configuration of the embedded microchannels and develop required guidelines and charts that facilitate the design of the AC-PMC plate used in hypersonic aircrafts.

^{*} Corresponding author. Tel.: +1 217 244 7648; fax: +1 217 244 0720.

E-mail address: geubelle@illinois.edu (P.H. Geubelle).

¹ Current address: Department of Mechanical and Aerospace Engineering, Ohio State University, Scott Laboratory, 201 West 19th Avenue, Columbus, OH 43210, USA.

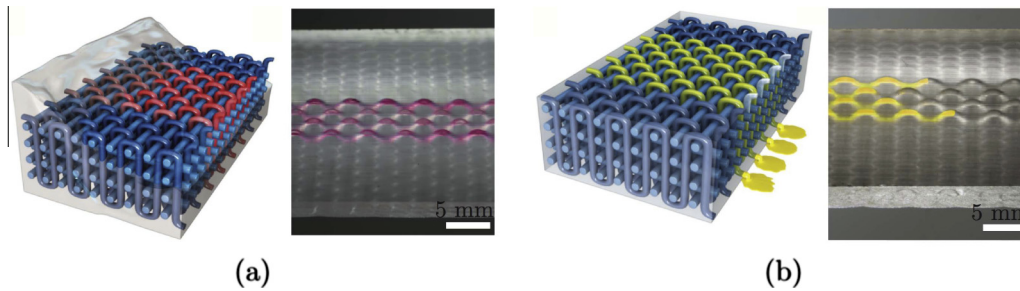


Fig. 1. Schematic and optical images of (a) sacrificial PLA fibers (shown in pink) embedded in a 3D woven glass/epoxy composite specimen and (b) hollow microchannels formed after evacuating the fibers, filled with a yellow fluid. (Adapted from [12]).

Actively-cooled materials with embedded networks of microchannels have been used for other high heat flux applications [13–15]. Due to manufacturing constraints, straight microchannels with or without branching are often employed for active cooling, as this configuration yields a high heat transfer efficiency even in the laminar regime [16]. Some studies have shown that introducing waviness in the microchannels leads to a better heat transfer performance at higher Reynolds numbers [17]. The impact of other geometric features on the thermal efficiency of the system, including the number, spacing, and cross-sectional porosity of microchannels and the arrangement of inlets and outlets, are also widely investigated [18–21]. In addition to their heat transfer performance, embedded networks are characterized by the inherent cost associated with the pressure drop needed to circulate the coolant through the microchannels [22,23]. Various techniques such as parametric studies and evolutionary algorithms are also used to determine the optimal configuration of microchannel heat sinks based on these parameters [24–26].

In the current study, which relies on a parametric design approach, the optimal configuration of the microchannels is determined such that it minimizes (i) the maximum temperature of the plate, (ii) the microchannel volume fraction, and (iii) the pressure head required to circulate the coolant in the microchannels. In addition to the microchannels configuration, we study the impact of a variety of other design parameters on the thermal response of the system, including the dimensions of the plate, microchannels spacing, applied thermal loads, boundary conditions (BCs), and the type and flow rate of the coolant. The greatest challenge in evaluating the thermal response of the AC-PMC plate with the standard Finite Element Method (FEM) is the need to create meshes that conform to the microchannels geometry. This becomes especially cumbersome in the design process, where one needs to create a new virtual model of the microvasculature for multiple microchannels configurations and domain dimensions. In this work, an Interface-enriched Generalized Finite Element Method (IGFEM) recently introduced by Soghrati et al. [27,28] is adopted to compute the temperature field. The IGFEM simplifies the design process as it uses finite element meshes that are independent of the problem morphology without affecting the accuracy of the solution. More details regarding the IGFEM thermal solver and its validation based on experiments conducted on an actively-cooled microvascular fin with sinusoidal microchannels can be found in [29].

It has been long shown that the Galerkin FEM (including the IGFEM) applied to convection-dominated flow problems suffers from spurious oscillations [30]. To address this issue, several stabilization methods including the Streamline Upwind Petrov–Galerkin (SUPG) [31,32], the Galerkin Least-Squares (GLS) [33,34], the variational multiscale (VMS) [35], and the residual-free bubble functions [36,37] methods have been proposed. In this work, the SUPG technique is adopted to stabilize the IGFEM and reduce the

spurious oscillations in the temperature field. It should be noted that, for steady convective heat transfer problems, all the aforementioned schemes add a similar stabilization term to the discretized form of the governing equations [38]. For a review of different stabilization techniques and their applications in other flow problems, please refer to [39–41].

The remainder of this manuscript is structured as follows: Section 2 introduces the geometry and BCs of the AC-PMC plate of interest together with the associated design parameters studied in this work. In Section 3, we present the governing equations for the convective heat transfer in actively-cooled microvascular materials and introduce the corresponding SUPG-stabilized IGFEM approximation. Finally, the impact of varied design parameters on the optimal microchannels configuration and the cooling efficiency of the PMC plate is investigated in Sections 4 and 5.

2. Problem description and design objectives

The schematic of the 3D woven glass fiber/epoxy matrix composite plate studied in this work is illustrated in Fig. 2. Fig. 3 shows the microvascular domain, where the parallel embedded sinusoidal microchannels (defined by the amplitude A and wavelength λ) have a diameter of $D = 500 \mu\text{m}$. The minimum distance between the microchannels centerline and the bottom surface of the plate is chosen to be $500 \mu\text{m}$. The coolant enters the microchannels with a flow rate of Q and an entrance temperature of $T_{\text{in}} = 20 \text{ }^\circ\text{C}$. Unless indicated otherwise, the coolant is water with the thermal conductivity, density, and specific heat of $\kappa_f = 0.6 \text{ W/m K}$, $\rho_f = 1000 \text{ kg/m}^3$, and $c_p = 4182.5 \text{ J/kg K}$, respectively. The temperature dependence of the dynamic viscosity of water μ_f is approximated using the Seeton relation [42],

$$\mu_f(T_f) = 2.414 \times 10^{-4} \frac{247.8}{T_f - 140}, \quad (1)$$

where T_f is the fluid temperature in degree Kelvin.

The microvascular PMC plate shown schematically in Fig. 3(a) has a thickness of $H = 6 \text{ mm}$, while its length L and width W are

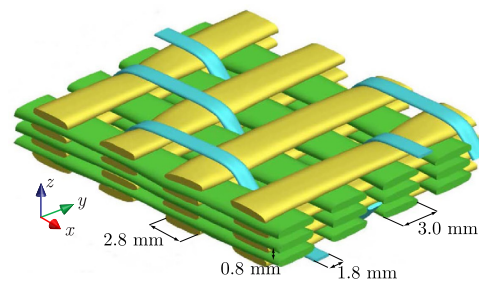


Fig. 2. Schematic of the microstructure of a unit cell of the 3D woven fiber structure of the PMC of interest. The warp (x), weft (y), and through-thickness (z) fiber tows are S2 glass and the matrix of the composite is epoxy.

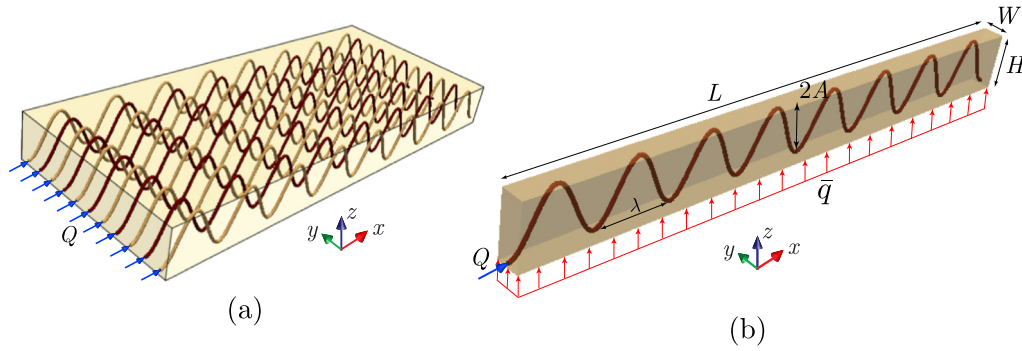


Fig. 3. (a) Schematic of the AC-PMC plate with parallel sinusoidal microchannels. (b) Reduced computational domain adopted by modeling a single embedded microchannel with periodic BC along the surfaces parallel to the microchannel centerline plane.

considered hereafter as design parameters. The boundary conditions consist of a constant heat flux applied over the bottom surface and insulated lateral surfaces. For the top surface of the plate, two types of BCs are considered: a prescribed constant temperature $\bar{T} = 20^\circ\text{C}$ and a convective BC with a heat transfer coefficient of $h = 25\text{ W/m}^2\text{ K}$ and an ambient temperature of $\bar{T}_\infty = 20^\circ\text{C}$. The value of h is evaluated experimentally via a thermal test on the PMC plate similar to that presented in [29]. As described in the FEM-based homogenization study in the Appendix, the effective thermal conductivities of the plate along the material principal axes are $\bar{\kappa}_{xx} = 0.47$, $\bar{\kappa}_{yy} = 0.45$, and $\bar{\kappa}_{zz} = 0.4\text{ W/m K}$. Taking advantage of the problem symmetry, we reduce the computational domain to that illustrated in Fig. 3(b) and adopt periodic BC along the surfaces of the repeating cell. The BCs along the top and bottom surfaces of this unit cell remain unchanged.

In the following sections, the impact of a variety of design parameters on the thermal response of the AC-PMC plate is studied. Some of these parameters, as shown in Fig. 3(b) and described in Table 1, include the wavelength λ and amplitude A of microchannels, length of the microvascular plate L , distance between two adjacent microchannels W , applied heat flux \bar{q} , and the coolant flow rate Q . Moreover, we investigate how the coolant type and the flow direction in the microchannels affect the thermal response of the system.

The design objectives of this work are to minimize the microchannel volume fraction and to maximize the flow and cooling efficiencies of the embedded microchannels (Fig. 3). To manage the flow efficiency, we aim to reduce the power needed to circulate the coolant, $P = \dot{m}\Delta p/\rho_f$, where Δp is the pressure drop in the microchannels. To evaluate Δp in a microchannel with a length of L_f , we adopt the classical Hagen-Poiseuille law [43],

$$\Delta p = \int_{L_f} \frac{128\bar{\mu}_f \dot{m} ds}{\rho_f \pi D^4}, \quad (2)$$

Table 1
Design parameters and their ranges studied for the design of the AC-PMC plate shown in Fig. 3.

Design parameter	Range of values/ options
Top surface boundary condition	Fixed temperature, convective
Flow direction in adjacent channels	Unidirectional, counter flow
Coolant flow rate Q (ml/min)	[0.1, 10]
microchannel wavelength A (mm)	[10, 20]
microchannel amplitude A (mm)	[0, 2.5]
microchannels spacing W (mm)	[1, 8]
Length of the PMC plate L (cm)	[10, 40]
Applied heat flux q (kW/m ²)	[10, 100]
Type of the coolant	Water, PAO, ethylene glycole

where $\dot{m} = \rho_f \pi D^2 Q/4$ is the mass flow rate, $\bar{\mu}_f$ is the average dynamic viscosity at each cross section, and ds is a longitudinal element along the microchannel centerline.

The main objective involved in the design of the AC-PMC plate is to maximize the *thermal efficiency* of the embedded network, defined as

$$\eta_T = 1 - \frac{T_{\max} - T_{\text{ref}}}{T_{\max}^0 - T_{\text{ref}}}. \quad (3)$$

In (3), $T_{\text{ref}} = 20^\circ\text{C}$ is the reference temperature of the composite, i.e., the temperature in the absence of an applied heat flux over the bottom surface of the plate. T_{\max} and T_{\max}^0 are the maximum temperature of the heated composite plate with and without coolant flow in the microchannels, respectively. Using the 1D conductive heat transfer equations, we can readily evaluate T_{\max}^0 for the fixed temperature and convective BC cases as $T_{\max}^0 = \bar{q}H/\bar{\kappa}_{zz} + T_{\text{ref}}$ and $T_{\max}^0 = \bar{q}H/\bar{\kappa}_{zz} + \bar{q}/h + T_{\text{ref}}$, respectively. Table 2 presents the values of T_{\max}^0 versus \bar{q} in the absence of the active cooling.

For a given heat flux \bar{q} , we can use (3) to evaluate the minimum thermal efficiency required to keep T_{\max} below a limiting value. For the composite plate of interest shown in Fig. 3, the highest sustainable temperature before observing significant degradation of the matrix is set at $T_{\max} \approx 300^\circ\text{C}$. As indicated in Table 2, the maximum temperature of the composite in the absence of the active cooling can be significantly higher than this allowable value. Fig. 4 illustrates the variations of the minimum thermal efficiency $\eta_{T,\min}$ required to ensure $T < T_{\max}$ (300°C) for different values of \bar{q} . For example, when $\bar{q} = 100\text{ kW/m}^2$, the actively-cooled system must at least achieve $\eta_{T,\min} = 82.3\%$ and $\eta_{T,\min} = 94.5\%$ for the fixed temperature and convective BC cases, respectively.

A key constraint involved in the active cooling process is the maximum allowable temperature of the coolant. For example, if water is used as the coolant, $T_{f,\max} = 100^\circ\text{C}$ (boiling point). To incorporate this constraint in the design of the microvascular plate, we define the *energy efficiency* as

$$\eta_E = \frac{\dot{m}c_p(T_{f,\text{out}} - T_{f,\text{in}})}{\bar{q}A_b}, \quad (4)$$

where $A_b = LW$ is the area of the plate bottom surface and $T_{f,\text{out}}$ and $T_{f,\text{in}}$ are the average coolant temperatures at the inlet and the outlet,

Table 2
Maximum temperature T_{\max}^0 in the PMC plate for different values of \bar{q} and the two choices of the top surface BC in the absence of flow in the microchannels.

Heat flux q (kW/m ²)		10	20	25	50	100
Tmax (°C)	Fixed temp. BC	170	320	395	770	1520
	Convective BC	527	1034	1288	2556	5091

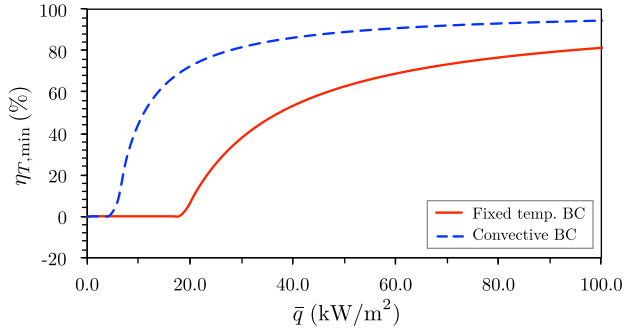


Fig. 4. Minimum thermal efficiency $\eta_{T,\min}$ required to maintain $T_{\max} < 300$ °C in the AC-PMC plate versus applied heat flux \bar{q} for the fixed temperature and convective BCs over the top surface.

respectively. η_E yields the ratio of the heat extracted by the coolant to the heat supplied to the system via \bar{q} . Also, the *coefficient of performance* is defined as

$$\gamma_P = \frac{\dot{m}c_p(T_{f,\text{out}} - T_{f,\text{in}})}{P} = \frac{\rho c_p(T_{f,\text{out}} - T_{f,\text{in}})}{\Delta p}, \quad (5)$$

the ratio of the extracted heat to the power needed to circulate the coolant in the microchannels. Providing a higher flow rate of the coolant allows extracting more heat from the plate, but also requires a higher pressure head, which increases the power consumption.

3. Thermal response: SUPG stabilized IGFEM solver

To evaluate the thermal response of the AC-PMC plate, we adopt the steady-state convection–diffusion equations. Consider an open domain $\Omega = \Omega_f \cup \Omega_s$ with boundary Γ and an outward unit normal vector \mathbf{n} , where Ω_f and Ω_s correspond to the fluid and the solid phases, respectively. The domain boundary is divided into three non-overlapping partitions Γ_T, Γ_q , and Γ_h to assign the fixed temperature, heat flux, and convective BCs, respectively. Given the thermal conductivity tensor $\boldsymbol{\kappa}$, fluid density ρ_f , fluid specific heat c_p , prescribed temperature, \bar{T} , applied heat flux \bar{q} , heat transfer coefficient h , and the ambient temperature \bar{T}_∞ , the strong form of the governing equations is described as

$$\begin{aligned} -\nabla \cdot (\boldsymbol{\kappa} \nabla T) + \rho_f c_p \mathbf{v} \cdot \nabla T &= 0 \quad \text{in } \Omega_f \\ \nabla \cdot (\boldsymbol{\kappa} \nabla T) &= 0 \quad \text{in } \Omega_s \\ T - \bar{T} &= 0 \quad \text{on } \Gamma_T \\ \boldsymbol{\kappa} \nabla T \cdot \mathbf{n} - \bar{q} &= 0 \quad \text{on } \Gamma_q \\ \boldsymbol{\kappa} \nabla T \cdot \mathbf{n} - h(\bar{T}_\infty - T) &= 0 \quad \text{on } \Gamma_h, \end{aligned} \quad (6)$$

where \mathbf{v} is the velocity field in the fluid phase. The small values of microchannel diameter D and coolant flow rate Q allow laminar flow with a fully-developed velocity profile in the microchannels given by [43]

$$\mathbf{v}(r) = \frac{8Q}{\pi D^2} \left(1 - \frac{2r}{D}\right)^2 \mathbf{n}_t, \quad (7)$$

where r is the distance from the centerline and \mathbf{n}_t is the tangential unit vector along the centerline of the microchannel.

Given the space of the weight functions $\mathcal{W} = \{w \in H_0^1(\bar{\Omega})\}$ and the solution functions $\mathcal{T} = \{T \in H^1(\bar{\Omega}) : T|_{\Gamma_T} = \bar{T}\}$, the weak form of (6) is expressed as: Find $T \in \mathcal{T}$ such that

$$\begin{aligned} \int_{\Omega} \nabla w \cdot \boldsymbol{\kappa} \nabla T \, d\Omega + \int_{\Omega_f} w \rho_f c_p \mathbf{v} \cdot \nabla T \, d\Omega + \int_{\Gamma_h} h w T \, d\Gamma \\ = \int_{\Gamma_h} h w \bar{T}_\infty \, d\Gamma + \int_{\Gamma_q} w \bar{q} \, d\Gamma \quad \forall w \in \mathcal{W}. \end{aligned} \quad (8)$$

Discretizing the domain $\Omega \cong \Omega^h$ into m non-conforming finite elements, the IGFEM approximation of (8) in each element is expressed as [27]

$$T^h(\mathbf{x}) = \sum_{i=1}^n N_i(\mathbf{x}) T_i + \sum_{j=1}^{n_{en}} S_j \psi_j(\mathbf{x}) \alpha_j. \quad (9)$$

The first term in (9) is the standard FEM part of the formulation, where $\{N_i(\mathbf{x})\}_{i=1}^n \subset \mathcal{T}^h$ are the n Lagrangian shape functions and T_i denotes the nodal value of the temperature. The second term in (9) is the contribution of the enrichment functions $\{\psi_j(\mathbf{x})\}_{j=1}^{n_{en}}$ used to capture the temperature gradient discontinuity along the fluid/solid interface. These enrichment functions are constructed as a linear combination of the Lagrangian shape functions of the integration sub-elements. For more information regarding the IGFEM formulation, convergence study, and applications, see [27,28].

In the Galerkin formulation [44] of the IGFEM, the weighting functions in (8) are similar to the trial functions adopted in (9) to approximate the temperature field, i.e., $w^h = \{N_i(\mathbf{x})\}_{i=1}^n, \psi_j(\mathbf{x})\}_{j=1}^{n_{en}}$. While this yields the optimal accuracy for evaluating the thermal response in the solid phase, the presence of the convection term in the fluid leads to an unstable formulation, which introduces spurious oscillations to the approximate field. The amplitude of these fictitious oscillations is a function of the element Peclet number [30],

$$Pe_k = \frac{\rho_f c_p |\mathbf{v}_k| h_k}{2\kappa_k}, \quad (10)$$

where $|\mathbf{v}_k|$ is the norm of the velocity vector and $\kappa_k = \|\boldsymbol{\kappa} \cdot \mathbf{v}_k\| / \|\mathbf{v}_k\|$ and h_k are the thermal conductivity and length of the element in the flow direction, respectively, with [38]

$$h_k = 2|\mathbf{v}_k| \left(\sum_{i=1}^n |\mathbf{v}_k \cdot \nabla N_i| \right)^{-1}. \quad (11)$$

To reduce the spurious oscillations in the temperature field using the SUPG scheme, the trial weighting functions are modified to place more weight on the upstream nodes as [31,32]

$$\tilde{w}^h = w^h + \tau \rho c_p \mathbf{v} \cdot \nabla w^h, \quad (12)$$

where τ is called the *stabilization parameter*. The second term in \tilde{w}^h induces an artificial diffusion in the IGFEM formation, which alleviates the under-diffusive solution obtained from the Galerkin method. For multi-dimensional problems, τ can be evaluated as [38]

$$\tau = \frac{h_k}{2\rho_f c_p |\mathbf{v}_k|} \left(\coth Pe_k - \frac{1}{Pe_k} \right). \quad (13)$$

Note that, for the radially varying velocity field present in the microchannels, τ is not constant and must be evaluated at each Gauss point of the integration sub-elements. The stabilized IGFEM approximation of (8) with first-order enrichment and Lagrangian shape functions is expressed as

$$\begin{aligned} \int_{\Omega} \nabla w^h \cdot \boldsymbol{\kappa} \nabla T^h \, d\Omega + \int_{\Omega_f} w^h \rho c_p \mathbf{v} \cdot \nabla T^h \, d\Omega + \int_{\Gamma_h} h w^h T^h \, d\Gamma \\ + \left[\int_{\Omega_f} \tau (\rho c_p \mathbf{v} \cdot \nabla w^h) (\rho c_p \mathbf{v} \cdot \nabla T^h) \, d\Omega \right] \\ = \int_{\Gamma_h} h w^h \bar{T}_\infty \, d\Gamma + \int_{\Gamma_q} w^h \bar{q} \, d\Gamma \quad \forall w^h \in \mathcal{W}^h, \end{aligned} \quad (14)$$

where the term in the square brackets corresponds to the SUPG stabilization.

Fig. 5 presents a comparison between the Galerkin and SUPG IGFEM approximations along the centerline of a straight microchannel. Both solutions are obtained using the same

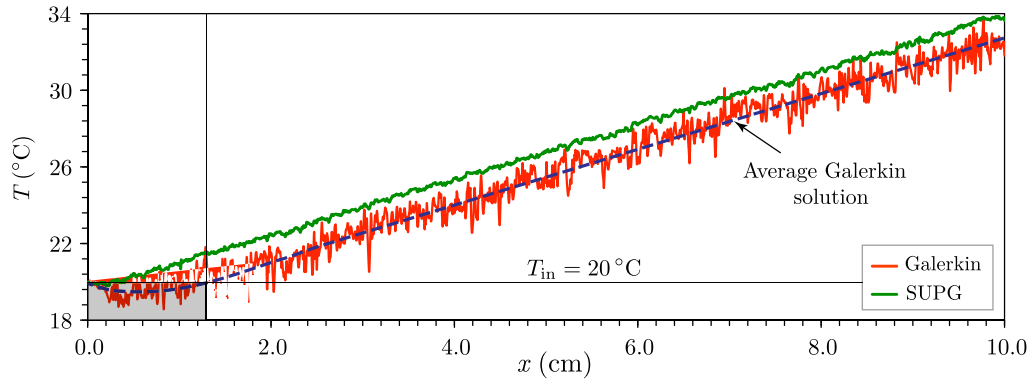


Fig. 5. Coolant temperature along the centerline of microchannel evaluated by the SUPG and Galerkin IGFEM solvers for the case $L = 10$ cm, $W = 1$ mm, $Q = 10$ ml/min, $\bar{q} = 100$ kW/m², and with the top surface convective BC. The dashed curve shows the average Galerkin solution, obtained by eliminating the spurious oscillations in the actual temperature profile. The shaded area corresponds to the region where the corresponding coolant temperature falls below its entrance temperature.

non-conforming tetrahedral mesh. As apparent in Fig. 5, the SUPG scheme substantially reduces the spurious oscillations. Furthermore, comparison with the analytical solution shows that the SUPG stabilized results are more accurate than those of the Galerkin method. To make a qualitative comparison, we can monitor the variation of the average coolant temperature profile obtained from the Galerkin IGFEM in Fig. 5, which drops below its entrance temperature $T_{in} = 20$ °C in the shaded area. Since the coolant temperature at the entrance is considerably lower than the initial temperature of the heated plate, it cannot become colder than T_{in} . On the other hand, the temperature profile approximated with the SUPG stabilized solver stays larger than T_{in} , which can better capture the physical behavior of the system.

4. Sinusoidal versus straight microchannels

The temperature fields evaluated with the stabilized IGFEM solver in the AC-PMC plate corresponding to varied microchannels configurations are depicted in Fig. 6. All the results shown in this figure are computed using the same non-conforming finite element mesh, for which the lowest maximum temperature appears in the domain with the straight embedded microchannel. In general, the optimal microchannel configuration is a function of the domain length L , coolant flow rate Q , and the top surface BC. In the remainder of this section, we study the impact of these parameters on the optimal configuration of the microchannels. In all numerical simulations presented hereafter, the microchannels spacing is set at $W = 1$ mm, unless mentioned otherwise.

The temperature profile along the lower edge of the domain, i.e., the location with the highest temperature in the entire plate, is illustrated in Fig. 7 for a plate with $L = 40$ cm, $\bar{q} = 10$ kW/m², and subjected to convective BC along the top surface. Four microchannel configurations are presented for two values of the flow rate: $Q = 0.1$ (Fig. 7(a)) and $Q = 1$ ml/min (Fig. 7(b)). As apparent in these figures, straight microchannels yield the lowest maximum temperature in the composite plate for both flow rates. Moreover, as we move from a low flow rate ($Q = 0.1$ ml/min) to a larger one ($Q = 1$ ml/min), the temperature profile associated with the straight microchannel provides a lower bound for the temperature obtained for sinusoidal microchannels. Note that, since sinusoidal-shape microchannels are longer than their straight counterparts, wavy microchannels yield higher void volume fraction and pressure drop (Eq. (2)). Therefore, for the microvascular plate with top surface convective BC and $L < 40$ cm, the straight microchannel configuration is optimal for all three objective functions.

Fig. 8 presents similar results as Fig. 7, but for the case of fixed temperature BC along the top surface. As for convective BC, the straight microchannel configuration yields the lowest maximum temperature when $Q = 1.0$ ml/min (Fig. 8(b)). However, as shown in Fig. 8(a), for a lower flow rate, $Q = 0.1$ ml/min, the sinusoidal microchannel with the smallest wavelength $\lambda = 10$ mm and the largest amplitude $A = 2.5$ mm yields the least maximum temperature. In this case, the sinusoidal configuration of the microchannel allows an effective redistribution of the heat between the top and the bottom surfaces of the plate, which leads to a periodic temperature profile. As illustrated in Fig. 8(a), the temperature associated with the straight microchannel is monotonically increasing and

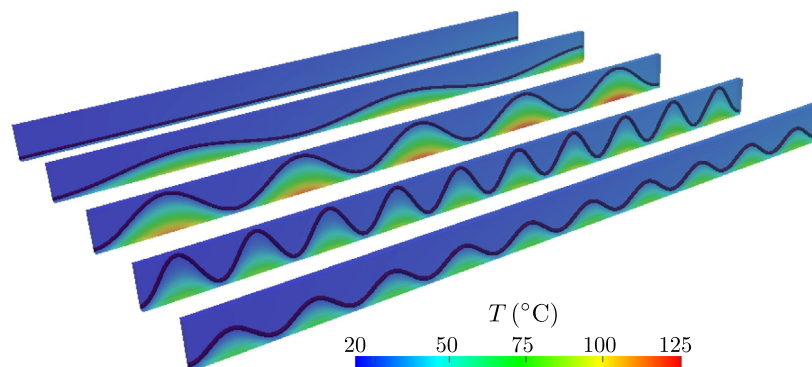
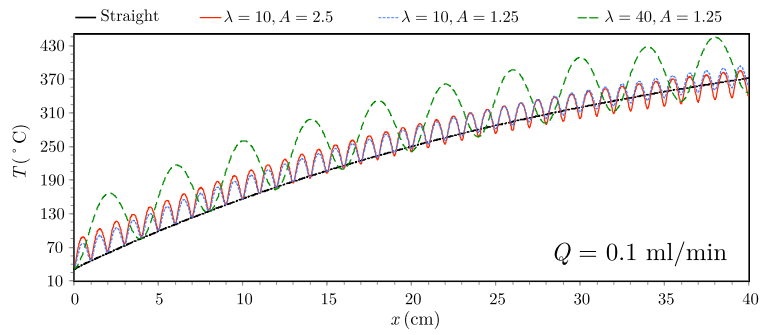
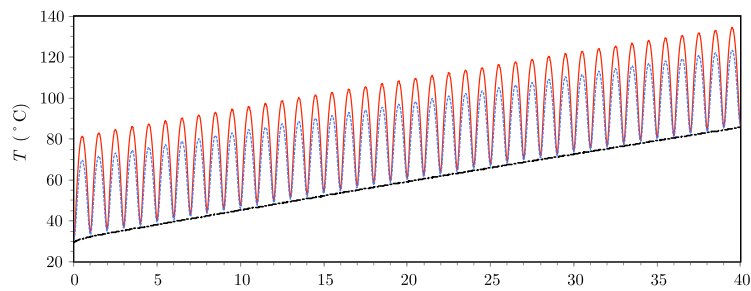


Fig. 6. Temperature field associated with different configurations of the embedded microchannels in an AC-PMC plate with $L = 10$ cm, $W = 1$ mm, $\bar{q} = 10$ kW/m², $Q = 1$ ml/min, and top surface convective BC.

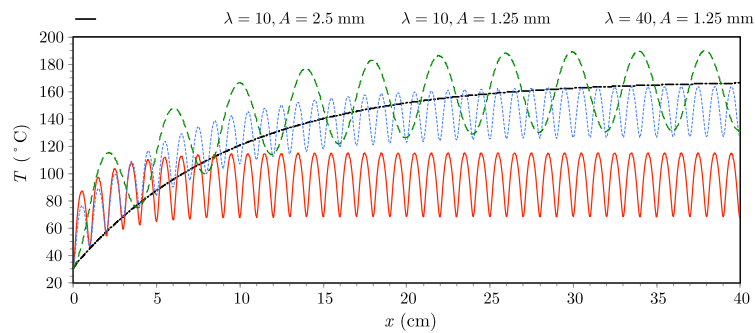


(a)

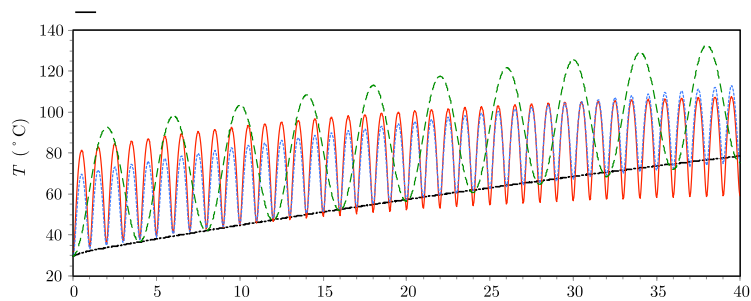


(b)

Fig. 7. Temperature profile associated with four microchannel configurations along the bottom edge of the domain for the convective BC case and $W = 1 \text{ mm}$, $q = 10 \text{ kW/m}^2$, and (a) $Q = 0.1$ and (b) $Q = 1.0 \text{ ml/min}$. The wavelength λ and amplitude A are given in mm.



(a)



(b)

Fig. 8. Similar description as Fig. 7, but with convective BC along the top surface.

eventually exceeds that of the sinusoidal microchannel at a *critical length* of $L_c = 8.56 \text{ cm}$. In other words, if $L > L_c = 8.56 \text{ cm}$, using the sinusoidal microchannel is more effective in reducing the maximum temperature of the composite and vice versa.

The impact of the coolant flow rate on the critical length of the plate for different values of λ and A is depicted in Fig. 9. As shown there, while L_c increases linearly with Q , it is independent of the magnitude of the applied heat flux. Moreover, for all three sinuso-

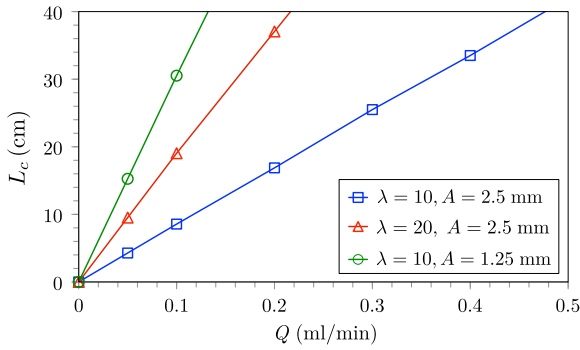


Fig. 9. Critical length L_c of the AC-PMC plate versus Q for a periodic cell with $W = 1$ mm and fixed temperature BC along its top surface. The straight microchannel configuration is optimal for minimizing T_{\max} when the length L of the plate is smaller than L_c .

dal microchannel configurations, L_c is larger than 40 cm when $Q = 0.5$ ml/min. The maximum value adopted for PMC plate length in this work is $L = 40$ cm, as using higher lengths leads to excessively large pressure drops in the microchannels. Furthermore, using a flow rate smaller than $Q = 0.5$ ml/min cannot effectively reduce T_{\max} for the high thermal loads expected in hypersonic aircrafts. Therefore, similar to the AC-PMC plate with the convective BC along its top surface, the straight microchannel is the optimal configuration for the case of fixed temperature BC when $Q > 0.5$ ml/min and $L < 40$ cm.

5. Design of the AC-PMC plate with straight microchannels

We now turn our attention on the impact of other design parameters presented in Table 1 on the thermal response of the AC-PMC plate with straight microchannels. The dependence of

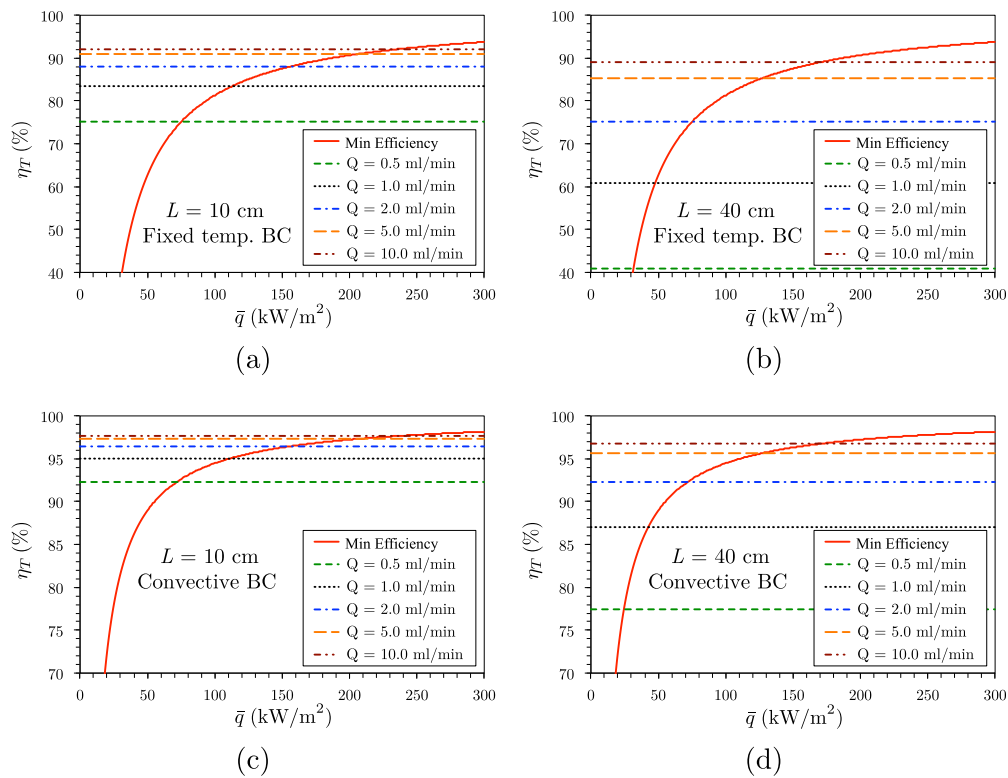


Fig. 10. Thermal efficiency η_T versus heat flux \bar{q} for different values of coolant flow rate Q : (a) Fixed temperature BC and $L = 10$ cm, (b) Fixed temperature BC and $L = 40$ cm, (c) Convective BC and $L = 10$ cm, (d) Convective BC and $L = 40$ cm. The solid curve corresponds to the minimum thermal efficiency needed to keep $T_{\max} < 30$ °C (Fig. 4).

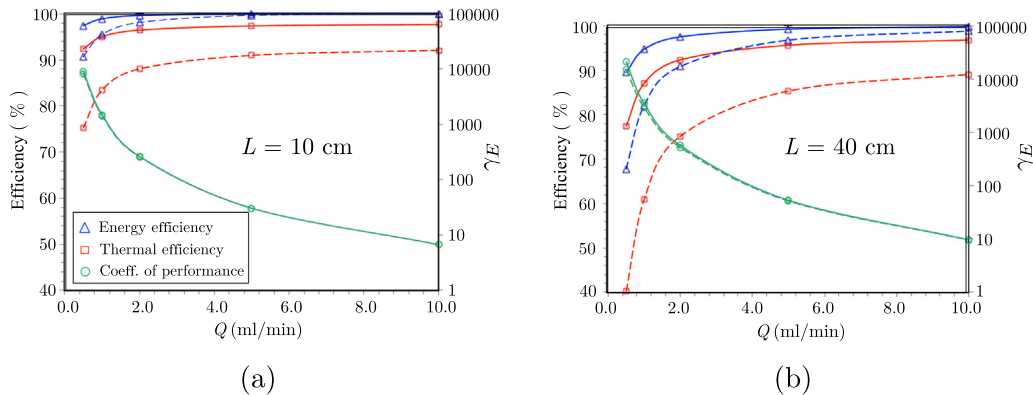


Fig. 11. Thermal efficiency η_T , energy efficiency η_E , and coefficient of performance γ_E versus flow rate Q for two PMC plate subjected to $\bar{q} = 100$ kW/m² and (a) $L = 10$ cm and (b) $L = 40$ cm. The solid and dashed lines show the results for convective and fixed temperature BC, respectively. The γ_E curves for convective and fixed BC cases are almost identical.

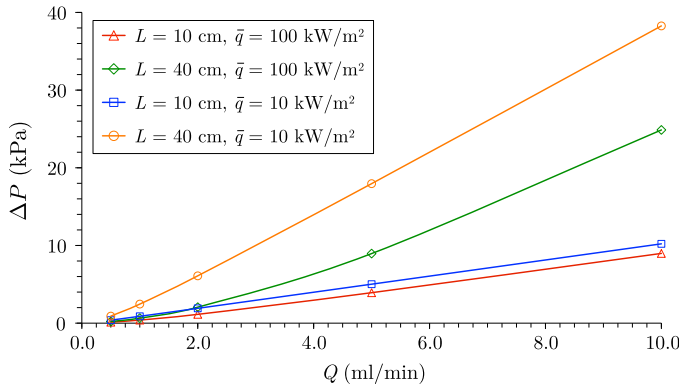


Fig. 12. Pressure drop Δp in the microchannels versus coolant flow rate Q for the AC-PMC plate with convective BC along the top surface.

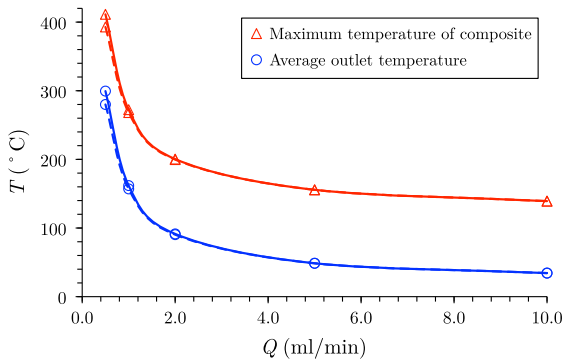


Fig. 13. T_{\max} and $T_{f,\text{out}}$ versus Q for a microvascular PMC plate with $L = 10$ cm, $W = 1$ mm, and $\bar{q} = 100$ kW/m². The solid and dashed lines correspond to convective and fixed temperature BCs, respectively.

the thermal efficiency η_T on the applied heat flux \bar{q} for different values of the flow rate Q is presented in Fig. 10 for $L = 10$ cm (Fig. 10(a) and (c)) and $L = 40$ cm (Fig. 10(b) and (d)). As described earlier, due to the linear response of the thermal problem and the definition of the thermal efficiency, η_T is independent of \bar{q} . Thus, the intersection between the computed η_T values and the minimum required thermal efficiency $\eta_{T,\text{min}}$ (red solid curve) for each flow rate Q yields the maximum allowable heat flux corresponding to $T_{\max} = 300$ °C. Conversely, it provides for a given \bar{q} , the value of the minimum flow rate Q needed to keep $T_{\max} < 300$ °C. For example, Fig. 10(c) shows that for a PMC plate with $L = 10$ cm, $\bar{q} = 100$ W/m², and the top surface convective BC, a flow rate of at least

$Q = 1$ ml/min is required to maintain $T_{\max} < 300$ °C. For a similar but longer domain with $L = 40$ cm, the minimum required flow rate must be increased to $Q = 5$ ml/min (Fig. 10(d)).

The variations of the thermal efficiency η_T , energy efficiency η_E , and the coefficient of performance γ_E versus the coolant flow rate for a microvascular plate with $\bar{q} = 100$ kW/m² are depicted in Fig. 11. The results presented in Fig. 11(a) and (b) are obtained for domains with $L = 10$ cm and $L = 40$ cm, respectively. Note that, while η_T and η_E are independent of \bar{q} , γ_E is not. η_T and η_E are measures of the maximum temperature of the composite and the average coolant temperature at the outlet, respectively, while γ_E yields the ratio of the heat convected out of the system to the cost of the active cooling. Fig. 11 shows that increasing Q increases η_T and η_E . However, γ_E decreases with an increasing Q as the power P is proportional to Q^2 , but the removed heat from the system is proportional to Q . Moreover, comparing Fig. 11(a) and (b) shows that although increasing the domain length from $L = 10$ to $L = 40$ cm has a negative impact on η_T and η_E , it leads to an increase in γ_E .

Before studying the impact of other design parameters on the thermal response of the AC-PMC plate, we analyze the cost of active cooling in more details. As mentioned in Section 2, the power P needed to circulate the coolant is proportional to Δp between the inlet and outlet of a microchannel. The variation of Δp versus Q for $L = 10$ and 40 cm and $\bar{q} = 10$ and 100 kW/m² are depicted in Fig. 12. Although these results are obtained for a PMC plate with the top surface convective BC, the results are almost identical for fixed temperature BC. As expected, using a larger Q increases Δp . However, due to the temperature dependence of the coolant dynamic viscosity μ given by (1), the relationship between Δp and Q is nonlinear. Thus, the value of \bar{q} has an important impact on the magnitude of the pressure drop. For instance, note the decrease in Δp for a plate with $L = 40$ cm as the heat flux is decreased from $\bar{q} = 10$ to 100 kW/m². It must be mentioned that the domain length value also has a nonlinear impact on the pressure drop. As depicted in Fig. 12, the increase in Δp associated with $L = 40$ cm is less than four times that for $L = 10$ cm.

The variations of the composite maximum temperature T_{\max} and the average coolant temperature at the outlet $T_{f,\text{out}}$ versus Q for a domain with $L = 10$ cm and subjected to $\bar{q} = 100$ kW/m² are illustrated in Fig. 13. As shown there, the impact of the top surface BC on the thermal response of the plate for higher flow rates is negligible. Fig. 13 can then be used to evaluate the minimum required value of Q to maintain T_{\max} and $T_{f,\text{out}}$ in the allowable ranges.

The impact of the domain length L on T_{\max} and $T_{f,\text{out}}$ for $\bar{q} = 100$ kW/m², top surface convective BC, and different values of Q is illustrated in Fig. 14. As shown there, both T_{\max} and $T_{f,\text{out}}$ are increasing linearly with L , where their slope is increasing with Q . Fig. 14 also shows that the maximum allowable length of the domain for a

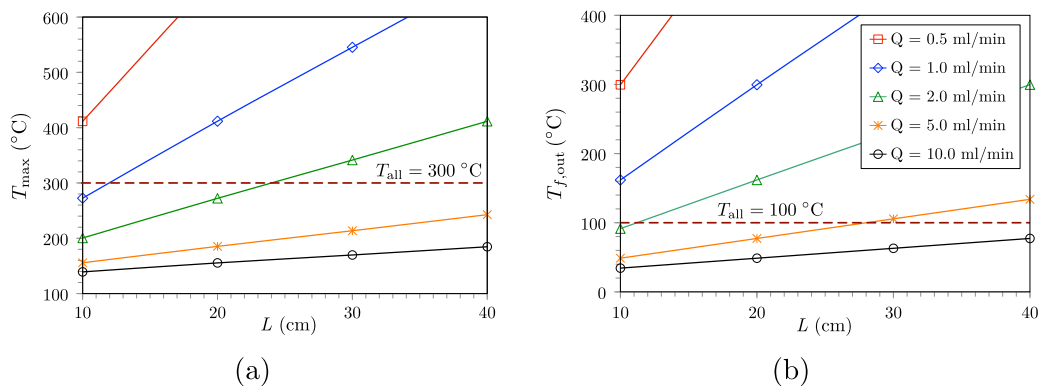


Fig. 14. (a) Maximum temperature of the composite T_{\max} and (b) coolant average outlet temperature $T_{f,\text{out}}$ versus the length L of the plate for $W = 1$ mm, $\bar{q} = 100$ kW/m², top surface convective BC, and different values of Q . The dotted horizontal lines denote the allowable values of T_{\max} and $T_{f,\text{out}}$ set at 300 °C and 100 °C, respectively.

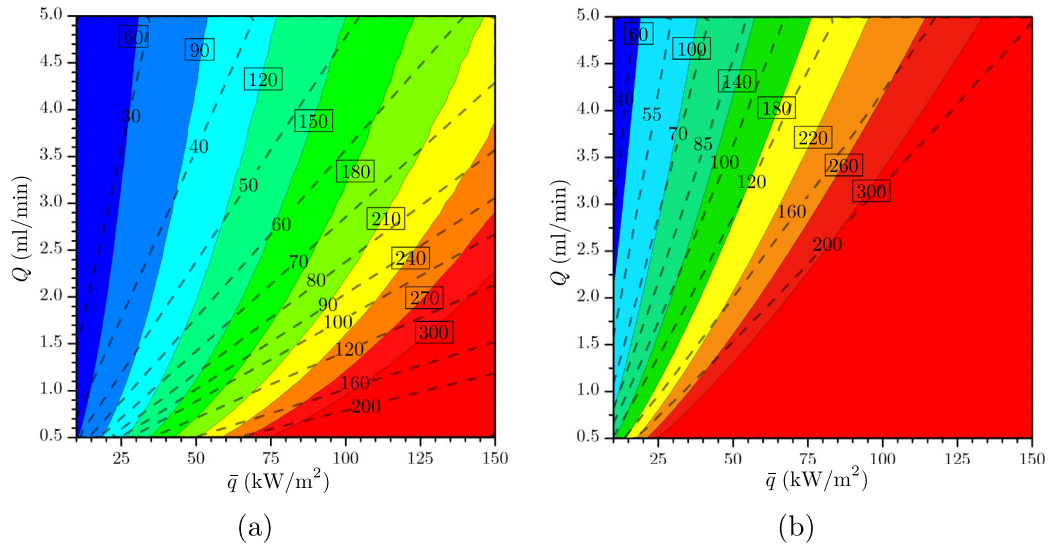


Fig. 15. $T_{f,out}$ and T_{max} versus Q and \bar{q} for a microvascular PMC plate with $W = 1$ mm, top surface convective BC, and (a) $L = 10$ cm and (b) $L = 40$ cm. The dashed and contour lines correspond to $T_{f,out}$ and T_{max} , respectively, with the contour values of T_{max} written in boxes.

Table 3

Material properties and allowable temperatures of three candidate coolants for the AC-PMC plate of interest, with $\alpha_Q = (\rho c_p)_{water} / (\rho c_p)_{coolant}$.

Coolant	c_p (kJ/kg K)	ρ (kg/m ³)	μ (kg/ms)		T_{all} (°C)	α_Q
			$T = 40$ °C	$T = 100$ °C		
Water	4183	1000	6.53×10^{-4}	2.80×10^{-4}	100	1
Polyalphaolefine	2220	809	4.45×10^{-3}	1.45×10^{-3}	161	2.33
Ethylene glycol	2440	1113	9.80×10^{-3}	1.98×10^{-4}	111	1.54

given value of Q is determined based on the maximum allowable temperature of the coolant ($T_{f,out} = 100$ °C) and not that of the composite ($T_{max} = 300$ °C).

We can generalize the results presented in Figs. 13 and 14 for evaluating T_{max} and $T_{f,out}$ in the form of the design maps shown in Fig. 15. In this figure, the solid contour lines represent the maximum temperature of the composite, while the dashed lines show the average coolant temperature at the outlet for different values of \bar{q} and Q . The contours for $T_{max} > 300$ °C are not shown since this temperature is considered as a physical limit for the polymer matrix. Fig. 15(a) and (b) illustrate the results for PMC plates with the convective BC along the top surface and $L = 10$ and $L = 40$ cm, respectively. Note that, except for slight differences at low flow rates, the results presented in Fig. 15 are identical for the fixed temperature BC.

The diagram presented in Fig. 15 can be used to design the AC-PMC plate by evaluating the minimum required flow rate Q

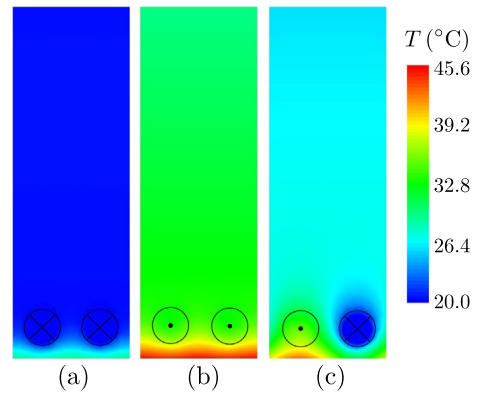


Fig. 17. Temperature field over the inlet and outlet surfaces of an AC-PMC plate with $W = 1$ mm, $L = 10$ cm, $\bar{q} = 10$ kW/m², and convective BC: (a) inlet and (b) outlet surfaces for the unidirectional flow and (c) inlet/outlet surfaces for the counter flow. The solid and dashed lines indicate the unidirectional and counter flow in microchannels, respectively.

for any value of applied heat flux \bar{q} . As referred to in Figs. 13 and 14, these results verify that the minimum required value of Q is determined by the constraint on maximum allowable temperature $T_{f,out}$ of the coolant (water), as the area covered by $T_{f,out} < 100$ °C is smaller than that covered by $T_{max} < 300$ °C for the range of design

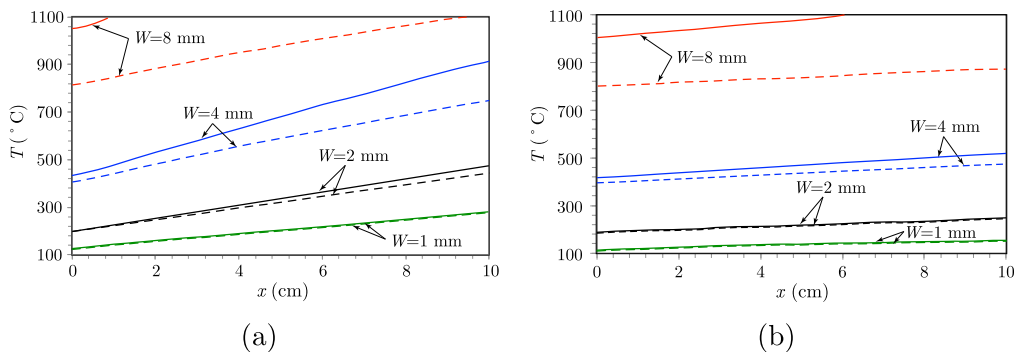


Fig. 16. Effect of microchannels spacing W on spatial temperature variation along the bottom edge of an AC-PMC plate with $\bar{q} = 100$ kW/m², $L = 10$ cm, and (a) $Q = 1$ and (b) $Q = 5$ ml/min. The solid and dashed lines correspond to the convective and fixed temperature BCs along the top surface of the plate, respectively.

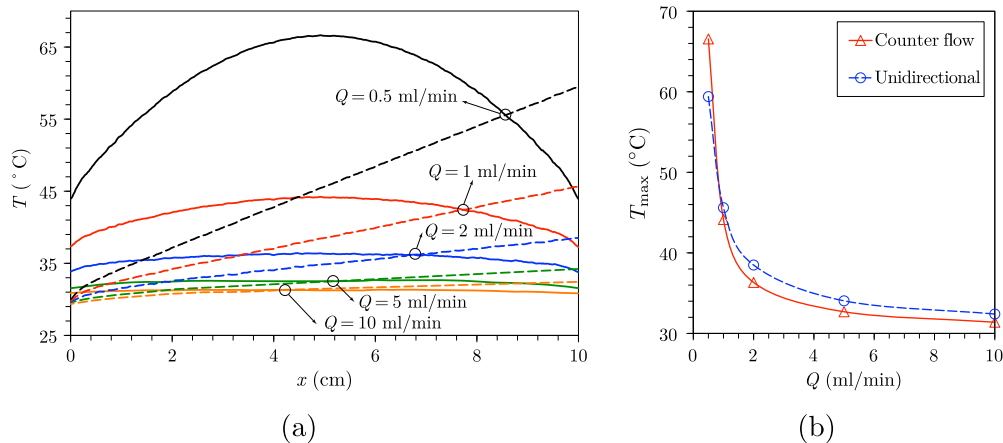


Fig. 18. Unidirectional versus counter flow solutions for $W = 1$ mm, $L = 10$ cm, $\bar{q} = 10$ kW/m², and top surface convective BC. (a) Temperature profiles along the bottom edge; (b) T_{max} versus Q . The solid and dashed curves denote the counter flow and unidirectional cases, respectively.

parameters considered in this work. As apparent in Fig. 15, satisfying the constraint on $T_{f, out}$ for water leads to a significant increase in the minimum required flow rate and thereby the cost of the active cooling. This suggests that using a different coolant with a larger maximum allowable temperature may reduce the cost of active cooling. The thermal properties of ethylene glycol (EG) and poly-alphaolefin (PAO) as two popular candidate coolants are presented in Table 3. The allowable temperature for these oil-based coolants are selected as their flash point, which is larger than the boiling point of water. However, according to Table 3, these coolants have a considerably lower specific heat and higher dynamic viscosity than water, which reduces the cooling efficiency and the coefficient of performance. Therefore, the impact of replacing water with either of the coolants given in Table 3 is not immediately obvious.

Converting the water-based design diagram presented in Fig. 15 to one used with other coolants can be achieved as follows: According to (6), the heat convection in the embedded microchannels is proportional to $\rho_f c_p \mathbf{v}$. Therefore, the amount of heat convected out of a microchannel is proportional to $\rho c_p Q / \bar{A}$, where \bar{A} is the microchannel cross section. For a new coolant, the flow rate can thus be scaled by a factor of $\alpha_Q = (\rho c_p)_{water} / (\rho c_p)_{coolant}$ such that $(\rho c_p Q / \bar{A})_{water} = (\rho c_p \alpha_Q Q / \bar{A})_{coolant}$ to yield the same thermal response. According to Table 3, the equivalent flow rate for PAO and EG are $\alpha_Q = 2.33$ and 1.54 times larger than that of water, while the corresponding increase in $T_{f, max}$ is only about 61% and 11%, respectively. Therefore, the minimum required flow rate obtained from Fig. 15 for each of these coolants will be larger than the required flow rate when using water. Moreover, the substantially (between three to five times) larger values of the dynamic viscosity μ of PAO and EG compared to water causes a substantial increase in the pressure drop. Therefore, among the three coolants investigated in this work, water appears to be the best choice for the design of the AC-PMC plate.

In the microvascular composite plates studied thus far, the distance between the microchannels centerlines was fixed at $W = 1$ mm. The impact of increasing W on the temperature profile along the bottom edge of a domain with $\bar{q} = 100$ kW/m² and $L = 10$ cm is depicted in Fig. 16 for $Q = 1$ and $Q = 5$ ml/min. Moreover, increasing W increases the impact of the top surface BC on the thermal response of the AC-PMC plate, as the temperature values for top surface convective BC become significantly higher than those of fixed temperature BC counterparts.

As a final design parameter, we study the thermal impact of unidirectional versus counter flow in the adjacent microchannels. Fig. 17 illustrates the temperature field over the inlet and outlet

surfaces of the microvascular plate for $Q = 1$ ml/min, $L = 10$ cm, $\bar{q} = 10$ kW/m², and convective BC over the top surface. As shown there, the temperature over the inlet/outlet surfaces of the domain with the counter flow is considerably lower than that over the outlet surface of the domain with the unidirectional flow. For the counter flow case, the cold fluid at the inlet absorbs the heat from the hot fluid in the adjacent microchannel, which can successfully reduce the temperature over the inlet/outlet surfaces.

The temperature profiles along the bottom edge and the maximum temperatures in the AC-PMC plate for different coolant flow rates obtained with unidirectional and counter flows are presented in Fig. 18. The microvascular domain studied in this figure has $L = 10$ cm, $\bar{q} = 10$ kW/m², and convective BC along the top surface. As expected, while the unidirectional flow leads to a monotonic increase of the temperature from the inlet to the outlet, the counter flow yields a symmetric temperature profile, with the maximum located in the middle of the specimen. Fig. 18(b) shows that the impact of the flow direction on the thermal response of the plate is a function of Q . For smaller flow rates ($Q < 1$ ml/min), using unidirectional flow is more effective in reducing T_{max} . However, for larger values of Q , T_{max} can be further reduced when using counter flow, due to the effective heat exchange between hot and cold coolants in the adjacent microchannels.

6. Conclusions

The computational design of an actively-cooled microvascular composite plate with sinusoidal and straight embedded microchannels was performed with the aid of an Interface-enriched Generalized Finite Element Method (IGFEM) solver. By eliminating the need to create meshes that conform to the microchannels geometry, the IGFEM significantly simplifies and speeds up the design process without affecting the accuracy of the solution. To eliminate the spurious oscillations in the field due to the convective heat transfer in the microchannels, the Streamline Upwind Petrov-Galerkin (SUPG) stabilization technique was also implemented. Several objective functions and constraints were considered, including the maximum temperature of the composite, maximum allowable temperature of the coolant, and the pressure drop in the microchannels. The design parameters included the microchannels configuration, length of the domain, microchannels spacing, coolant type, flow rate, applied heat flux, top surface BCs, and the flow direction in adjacent microchannels. The thermal and energy efficiencies and the coefficient of performance of the AC-PMC plate

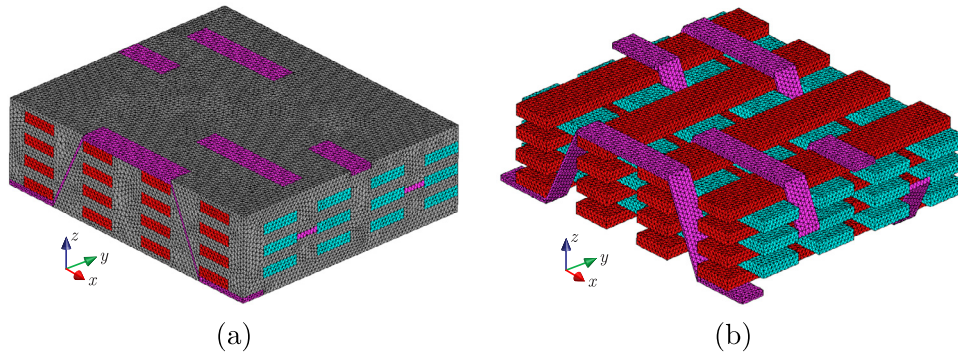


Fig. A.1. Finite element meshes in (a) the entire domain and (b) glass fiber tows for evaluating the effective thermal properties of the composite unit cell as shown in Fig. 2.

were evaluated for different values of the heat flux and flow rate. The key observations of this study are as follows:

- For an AC-PMC plate with $Q > 0.5$ ml/min and $L < 40$ cm, the straight microchannel is the optimal configuration regardless of the BC along the top surface of the plate.
- The maximum allowable temperature of the coolant determines the flow rate needed for the active cooling.
- Compared to oil-based coolants ethylene glycole and polyalphaolefin, water yields the lowest cost of the active cooling and therefore is a better choice for the coolant.
- At higher flow rates ($Q > 1$ ml/min), counter flow in the adjacent microchannels improves the cooling efficiency.

Acknowledgement

This work has been supported by the Air Force Office of Scientific Research Multidisciplinary University Research Initiative on *Functionally Graded Hybrid Composites* (FA9550-09-1-0686).

Appendix A. PMC plate effective thermal conductivities

A combined analytical/FEM-based approach is used to compute the effective thermal properties of the PMC plate in the absence of embedded microchannels. The thermal conductivity of the epoxy matrix and S2 glass fibers are $\kappa_e = 0.23$ and $\kappa_g = 1.45$ W/m K, respectively. To determine the effective thermal conductivities of the composite, we first evaluate those of the glass fiber tows. Each fiber tow containing the glass fibers infiltrated with the epoxy resin is modeled as a transversely isotropic unidirectional composite. The effective thermal conductivities along the principal axes of these fiber tows are given by [45]

$$\begin{aligned} \bar{\kappa}_{11} &= V_g \kappa_g + (1 - V_g) \kappa_e, & \bar{\kappa}_{22} &= \bar{\kappa}_{33} \\ &= \kappa_e \left[1 - \frac{2V_g}{v + V_g - \frac{3V_g^4}{v^2 \pi^4} S^2} \right], \end{aligned} \quad (\text{A.1})$$

where $S = 0.032\pi^4$, $v = \frac{\kappa_e + \kappa_g}{\kappa_e - \kappa_g}$, and V_g is the volume fraction of glass fibers, which equals $V_g \approx 0.6$ for the PMC of interest [12]. According to (A.1), we then have $\bar{\kappa}_{11} = 0.962$ and $\bar{\kappa}_{22} = \bar{\kappa}_{33} = 0.576$ W/m K as effective thermal conductivities of the fiber tows.

The homogenized thermal properties of the fiber tows are then used to determine the effective thermal conductivities of the woven composite. To model the composite microstructure (Fig. 2), we implement an FEM-based approach using the finite element meshes shown in Fig. A.1. To evaluate the effective properties in each material principal direction, numerical simulations with various BCs are performed. For example, the effective thermal

conductivity of the plate in the z direction, $\bar{\kappa}_{zz}$, is computed by assigning a uniform heat flux \bar{q}_b along the bottom surface, a constant temperature \bar{T}_t along the top surface, and insulating the other surfaces as [46],

$$\bar{\kappa}_{zz} = \frac{\bar{q}_b H}{\bar{T}_b - \bar{T}_t}, \quad (\text{A.2})$$

where the temperature along the bottom surface in the exact solution is replaced with the average temperature \bar{T}_b evaluated from the FEM approximation. Following the same procedure for $\bar{\kappa}_{xx}$ and $\bar{\kappa}_{yy}$ yields the effective properties presented in Section 2, i.e., $\bar{\kappa}_{xx} = 0.47$, $\bar{\kappa}_{yy} = 0.45$, and $\bar{\kappa}_{zz} = 0.4$ W/m K.

References

- [1] M.A. Burns, B.N. Johnson, S.N. Brahmaandra, K. Handique, J.R. Webster, M. Krishnan, T.S. Sammarco, P.M. Man, D.JonesD. Heldsinger, C.H. Mastrangelo, D.T. Burke, An integrated nanoliter DNA analysis device, *Science* 282 (1998) 484–487.
- [2] A. Strömberg, A. Karlsson, F. Ryttsén, M. Davidson, D.T. Chiu, O. Orwar, Microfluidic device for combinatorial fusion of liposomes and cells, *Anal. Chem.* 73 (2001) 126–130.
- [3] N.L. Jeon, S.K.W. Dertinger, D.T. Chiu, I.S. Choi, A.D. Strook, G.M. Whitesides, Generation of solution and surface gradients using microfluidic systems, *Langmuir* 16 (2000) 8311–8316.
- [4] Y. Wang, G. Yuan, Y.K. Yoon, M.G. Allen, S.A. Bidstrup, Active cooling substrates for thermal management of microelectronics, *IEEE Trans. Compon. Packag. Technol.* 28 (3) (2005) 477–483.
- [5] X. Wei, Y. Joshi, M.K. Patterson, Experimental and numerical study of a stacked microchannel heat sink for liquid cooling of microelectronic devices, *J. Heat Transfer* 129 (10) (2007) 1432–1444.
- [6] R.B. Oueslati, D. Therriault, S. Martel, PCB-integrated heat exchanger for cooling electronics using microchannels fabricated with the direct-write method, *IEEE Trans. Compon. Packag. Technol.* 31 (4) (2008) 869–874.
- [7] V.G. Pastukhov, Y.F. Maidanik, C.V. Vershinin, M.A. Korukov, Miniature loop heat pipes for electronics cooling, *Appl. Therm. Eng.* 23 (9) (2003) 1125–1135.
- [8] D. Therriault, S.R. White, J.A. Lewis, Chaotic mixing in three-dimensional microvascular networks fabricated by direct-write assembly, *Nat. Mater.* 2 (2003) 256–271.
- [9] J. Lewis, Direct writing of 3D functional materials, *Adv. Funct. Mater.* 16 (17) (2006) 2193–2204.
- [10] K.S. Toohy, N.R. Sottos, J.A. Lewis, J.S. Moore, S.R. White, Self-healing materials with microvascular networks, *Nat. Mater.* 6 (2007) 581–585.
- [11] S.C. Olugebefola, A.M. Aragón, C.J. Hansen, A.R. Hamilton, B.D. Kozola, W. Wu, P.H. Geubelle, J.A. Lewis, N.R. Sottos, S.R. White, Polymer microvascular network composite, *J. Compos. Mater.* 44 (22) (2010).
- [12] A.P. Esser-Kahn, P.R. Thakre, H. Dong, J. Patrick, N.R. Sottos, J.S. Moore, S.R. White, Three dimensional microvascular fiber-reinforced composites, *Adv. Mater.* 23 (32) (2011) 3654–3658.
- [13] E.S. Cho, J.W. Choi, J.S. Yoon, M.S. Kim, Experimental study on microchannel heat sinks considering mass flow distribution with non-uniform heat flux conditions, *Int. J. Heat Mass Transfer* 53 (9–10) (2010) 2159–2168.
- [14] C.Y. Zhao, T.J. Lu, Analysis of microchannel heat sinks for electronics cooling, *Int. J. Heat Mass Transfer* 45 (24) (2002) 4857–4869.
- [15] X.L. Xie, Z.J. Liu, Y.L. He, W.Q. Tao, Numerical study of laminar heat transfer and pressure drop characteristics in a water-cooled minichannel heat sink, *Appl. Therm. Eng.* 29 (1) (2009) 64–74.
- [16] A. Lee, V. Timchenko, G.H. Yeoh, J.A. Reizes, Three-dimensional modelling of fluid flow and heat transfer in micro-channels with synthetic jet, *Int. J. Heat Mass Transfer* 55 (1–3) (2012) 198–213.

- [17] Y. Sui, C.J. Teo, P.S. Lee, Y.T. Chew, C. Shu, Fluid flow and heat transfer in wavy microchannels, *Int. J. Heat Mass Transfer* 53 (13–14) (2010) 2760–2772.
- [18] X.F. Peng, B.X. Wang, G.P. Peterson, H.B. Ma, Experimental investigation of heat transfer in flat plates with rectangular microchannels, *Int. J. Heat Mass Transfer* 38 (1) (1995) 127–137.
- [19] H.-C. Chiu, J.-H. Jang, H.-W. Yeh, M.-S. Wu, The heat transfer characteristics of liquid cooling heatsink containing microchannels, *Int. J. Heat Mass Transfer* 54 (1–3) (2011) 34–42.
- [20] B. Agostini, M. Fabbri, J.E. Park, L. Wojtan, J.R. Thome, B. Michel, State of the art of high heat flux cooling technologies, *Heat Transfer Eng.* 28 (4) (2007) 258–281.
- [21] A.W. Mauro, J.R. Thome, D. Toto, G.P. Vanoli, Saturated critical heat flux in a multi-microchannel heat sink fed by a split flow system, *Exp. Therm. Fluid Sci.* 34 (1) (2010) 81–92.
- [22] W. Qu, I. Mudawar, Experimental and numerical study of pressure drop and heat transfer in a single-phase micro-channel heat sink, *Int. J. Heat Mass Transfer* 45 (12) (2002) 2549–2565.
- [23] M.I. Hasan, A.A. Rageb, M. Yaghoubi, H. Homayoni, Influence of channel geometry on the performance of a counter flow microchannel heat exchanger, *Int. J. Therm. Sci.* 48 (8) (2009) 1607–1618.
- [24] J.H. Ryu, D.H. Choi, S.J. Kim, Numerical optimization of the thermal performance of a microchannel heat sink, *Int. J. Heat Mass Transfer* 45 (13) (2002) 2823–2827.
- [25] Kwasi Foli, Tatsuya Okabe, Markus Olhofer, Yaochu Jin, Bernhard Sendhoff, Optimization of micro heat exchanger: Cfd, analytical approach and multi-objective evolutionary algorithms, *Int. J. Heat Mass Transfer* 49 (5–6) (2006) 1090–1099.
- [26] H.-S. Kou, J.-J. Lee, C.-W. Chen, Optimum thermal performance of microchannel heat sink by adjusting channel width and height, *Int. Commun. Heat Mass Transfer* 35 (5) (2008) 577–582.
- [27] S. Soghrati, A.M. Aragón, C.A. Duarte, P.H. Geubelle, An interface-enriched generalized finite element method for problems with discontinuous gradient fields, *Int. J. Numer. Methods Eng.* 89 (8) (2012) 991–1008.
- [28] S. Soghrati, P.H. Geubelle, A 3D interface-enriched generalized finite element method for weakly discontinuous problems with complex internal geometries, *Comput. Methods Appl. Mech. Eng.* 217–220 (2012) 46–57.
- [29] S. Soghrati, P.R. Thakre, S.R. White, N.R. Sottos, P.H. Geubelle, Computational modeling and design of actively-cooled microvascular materials, *Int. J. Heat Mass Transfer* 55 (19–20) (2012) 5309–5321.
- [30] J. Donea, A. Huerta, *Finite Element Methods for Flow Problems*, Wiley, 2003.
- [31] A.N. Brooks, T.J.R. Hughes, Streamline upwind/Petrov–Galerkin formulations for convection dominated flows with particular emphasis on the incompressible Navier–Stokes equations, *Comput. Methods Appl. Mech. Eng.* 32 (1982) 199–259.
- [32] T.J.R. Hughes, T.E. Tezduyar, Finite element methods for first-order hyperbolic systems with particular emphasis on the compressible euler equations, *Comput. Methods Appl. Mech. Eng.* 45 (1984) 217–284.
- [33] T.J.R. Hughes, L.P. Franca, M. Balestra, A new finite element formulation for computational fluid dynamics: V. Circumventing the Babuska–Brezzi condition: a stable Petrov–Galerkin formulation of the stokes problem accommodating equal-order interpolations, *Comput. Methods Appl. Mech. Eng.* 59 (1) (1986) 85–99.
- [34] L.P. Franca, S.L. Frey, Stabilized finite element methods: I application to advection-diffusion model, *Comput. Methods Appl. Mech. Eng.* 95 (2) (1992) 253–276.
- [35] T.J.R. Hughes, Multiscale phenomena: Green's functions, the Dirichlet-to-Neumann formulation, subgrid scale models, bubbles and the origins of stabilized methods, *Comput. Methods Appl. Mech. Eng.* 127 (1995) 387–401.
- [36] F. Brezzi, M.O. Bristeau, L.P. Franca, M. Mallet, G. Roge, A relationship between stabilized finite element methods and the Galerkin method with bubble functions, *Comput. Methods Appl. Mech. Eng.* 96 (1) (1992) 117–129.
- [37] F. Brezzi, D. Marini, A. Russo, Applications of the pseudo residual-free bubbles to the stabilization of convection-diffusion problems, *Comput. Methods Appl. Mech. Eng.* 166 (1998) 51–63.
- [38] T.P. Fries, H.G. Matthies, A review of Petrov–Galerkin stabilization approaches and an extension to meshfree methods, *Sci. Comput.*, 2004.
- [39] A. Masud, R. Calderer, A variational multiscale stabilized formulation for the incompressible Navier–Stokes equations, *Comput. Mech.* 44 (2) (2009) 145–160.
- [40] L.P. Franca, A. Neslitturk, On a two-level finite element method for the incompressible Navier–Stokes equations, *Int. J. Numer. Methods Eng.* 52 (2001) 433–453.
- [41] E. Oñate, A stabilized finite element method for incompressible viscous flows using a finite increment calculus formulation, *Comput. Methods Appl. Mech. Eng.* 182 (3–4) (2000) 355–370.
- [42] C.J. Seeton, Viscosity-temperature correlation for liquids, *Tribol. Lett.* 22 (1) (2006).
- [43] C.A. Brebbia, A. Ferrante, *Computational Hydraulics*, Butterworths, 1983.
- [44] O.C. Zienkiewicz, R.L. Taylor, J.Z. Zhu, *The Finite Element Method: Its Basis and Fundamentals*, Elsevier, 2005.
- [45] D.J. Radcliffe, H.M. Rosenberg, The thermal conductivity of glass-fibre and carbon-fibre/epoxy composites from 2 to 80 K, *Cryogenics* 22 (5) (1982) 245–249.
- [46] M.R. Islam, A. Pramila, Thermal conductivity of fiber reinforced composites by the FEM, *J. Compos. Mater.* 33 (18) (1999) 1699–1715.